Structure of the Calvin-Benson-Bassham sedoheptulose-1,7-bisphosphatase from the model microalga *Chlamydomonas reinhardtii*

Théo Le Moigne[1,2], Martina Santoni[1,3], Lucile Jomat[1], Stéphane D. Lemaire[1], Mirko Zaffagnini[3], Nicolas Chéron[4], Julien Henri[1,*]

1. Sorbonne Université, CNRS, Laboratoire de Biologie Computationnelle et Quantitative UMR 7238, Institut de Biologie Paris-Seine, 4 Place Jussieu, Paris F-75005, France

2. Faculty of Sciences, Doctoral School of Plant Sciences, Université Paris-Saclay, Saint-Aubin F-91190, France

3. Department of Pharmacy and Biotechnology, University of Bologna, Via Irnerio 42, Bologna I-40126, Italy

4. PASTEUR, Département de chimie, École Normale Supérieure (ENS), PSL University, Sorbonne Université, CNRS UMR8640, 75005 Paris, France

*corresponding author

e-mail: julien.henri@sorbonne-universite.fr

Phone: +33144276606

ORCID: Théo Le Moigne 0000-0003-2313-3052; Martina Santoni 0009-0005-2466-5327, Stéphane D. Lemaire 0000-0001-6442-0547, Mirko Zaffagnini 0000-0001-5115-0859, Nicolas Chéron 0000-0002-4090-5897; Julien Henri 0000-0003-0772-8881

Abstract

The Calvin-Benson-Bassham cycle (CBBC) performs carbon fixation in photosynthetic organisms. Among the eleven enzymes that participate in the pathway, sedoheptulose-1,7-bisphosphatase (SBPase) is expressed in photo-autotrophs and catalyzes the hydrolysis of sedoheptulose-1,7-bisphosphate (SBP) to sedoheptulose-7-phosphate (S7P). SBPase, along with nine other enzymes in the CBBC, contributes to the regeneration of ribulose-1,5-bisphosphate, the carbon-fixing co-substrate used by ribulose-1,5-bisphosphate carboxylase/oxygenase (Rubisco). The metabolic role of SBPase is restricted to the CBBC, and a recent study revealed that the three-dimensional structure of SBPase from the moss *Physcomitrium patens* was found to be similar to that of fructose-1,6-bisphosphatase (FBPase), an enzyme involved in both CBBC and neoglucogenesis. In this study we report the first structure of an SBPase from a chlorophyte, the model unicellular green microalga *Chlamydomonas reinhardtii*. By combining experimental and computational structural analyses, we describe the topology, conformations and quaternary structure of *Chlamydomonas reinhardtii* SBPase (*Cr*SBPase). We identify active site residues and locate sites of redox- and phospho-post-translational modifications that contribute to enzymatic functions. Finally, we observe that *Cr*SBPase adopts distinct oligomeric states that may dynamically contribute to the control of its activity.

Introduction

Photosynthetic carbon fixation is performed by eleven enzymes that collectively operate the Calvin-Benson-Bassham cycle (CBBC) (Calvin 1962, Johnson 2016), wherein Rubisco plays the prominent role in catalyzing fixation of inorganic carbon onto a pentose acceptor: ribulose-1,5-bisphosphate (RuBP). The net gain of the CBBC is one triose in the form of glyceraldehyde-3-phosphate (G3P) for every three carboxylation reactions catalyzed by Rubisco (Johnson and Alric 2013). Regeneration of RuBP is ensured by the other ten enzymes of the CBBC, among which phosphoribulokinase (PRK) and sedoheptulose-1,7-bisphosphatase (SBPase) are the only enzymes that are exclusively involved in this pathway. The remaining eight enzymes are paralogs of those involved in cytoplasmic glycolysis,

50 gluconeogenesis or the pentose-phosphate pathway. Hence, Rubisco, PRK, and SBPase are expressed
51 in photosynthetic organisms and fulfill biochemical functions so far uniquely attributed to the
52 photosynthetic carbon fixation.
53 Pioneering studies on SBPase were carried out using the native enzyme purified from wheat
54 chloroplasts (Woodrow 1982) and corn leaves (Nishizawa and Buchanan 1981), allowing quantitative
55 assays of its catalytic function. This enzyme catalyzes the hydrolysis of sedoheptulose-1,7-
56 bisphosphate (SBP) into sedoheptulose-7-phosphate (S7P) and requires magnesium ions for both
57 catalysis and activation. In addition, SBPase activity is modulated by pH and redox switching
58 mechanisms (Anderson 1974, Woodrow and Walker 1980, Cadet and Meunier 1988). Redox control
59 is exerted through dithiol/disulfide interchanges dependent upon the ferredoxin-thioredoxin cascade
60 arising from the activity of the illuminated photosystems (Schürmann and Buchanan 1975). In
61 tobacco leaf extracts, SBPase reaches its maximal activity after 10 minutes illumination (Zimmer,
62 Swart et al. 2021), and this activation kinetics is consistent with the slow reduction pattern of
63 *Arabidopsis* SBPase *in vitro* (Yoshida and Hisabori 2018).
64 The crystal structure of SBPase from the moss *Physcomitrium patens* (*Pp*SBPase) has been solved at a
65 resolution of 1.3 Å (Protein Data Bank entry : 5iz3) (Gutle, Roret et al. 2016). *Pp*SBPase fold is highly
66 similar to that of moss fructose-1,6-bisphosphatase (FBPase), yet the protein was shown to
67 distinctively oligomerize as a homodimer and to form a disulfide bridge in a different motif than that
68 found in plant FBPase (Chiadmi, Navaza et al. 1999) (Gütle, Roret et al. 2016). In spite of their
69 homology, the sequences of FBPase and SBPase seem to have evolved different regulatory and
70 catalytic properties that allow different contributions to the CBBC. Indeed, both enzymes specifically
71 recognize their respective 6-carbon and 7-carbon sugar substrates (*i.e.*, fructose-1,6-bisphosphate
72 and SBP, respectively), with only SBPase capable to hydrolyze the other substrate with a resulting
73 catalysis lower than that measured with SBP (Gütle, Roret et al. 2016). To date, the structural
74 components contributing to active site selectivity (*i.e.*, substrate recognition) can be retrieved from
75 two studies reporting the crystal structure of the dual function fructose-1,6-

76 bisphosphatase/sedoheptulose-1,7-bisphosphatase (F/SBPase) from *Thermosynechococcus*
77 *elongatus* in complex with SBP (Cotton, Kabasakal et al. 2015) and from *Synechocystis* sp. PCC 6803 in
78 complex with FBP (PDB entry 3RPL). Recently, it was proposed that the CBBC can bypass fructose-1,6-
79 bisphosphate (FBP) altogether, by only relying on SBP, glycolysis and the oxidative pentose-
80 phosphate pathway paralogs to regenerate the substrate of Rubisco (Ohta 2022).
81 Several studies have reported that SBPase, along with Rubisco, FBPase, aldolase and transketolase,
82 constitute a metabolic bottleneck for the CBBC ((Raines 2022) and references therein).
83 Overexpression of SBPase was found to effectively enhance photosynthesis and growth in plants
84 (Lefebvre, Lawson et al. 2005, Feng, Han et al. 2007, Feng, Wang et al. 2007, Rosenthal, Locke et al.
85 2011, Simkin, Lopez-Calcagno et al. 2017) and in the green microalga *Chlamydomonas reinhardtii*
86 (Hammel, Sommer et al. 2020), indicating that SBPase can be considered as a limiting factor for the
87 photosynthetic carbon fixation. Based on these evidences, it is plausible to consider that SBPase is a
88 good target to improve the photosynthetic capacity by means of metabolic engineering coupled to
89 synthetic biology (Kubis and Bar-Even 2019), especially in the experimentally convenient multi-omic
90 model alga Chlamydomonas (Mettler, Muhlhaus et al. 2014, Schmollinger, Mühlhaus et al. 2014).
91 In Chlamydomonas, SBPase is encoded by a single nuclear gene (Cre03.g185550), and the protein
92 (Uniprot entry P46284) is addressed to the chloroplast by a 54-residue amino-terminal peptide
93 (Emanuelsson, Brunak et al. 2007, Almagro Armenteros, Salvatore et al. 2019). SBPase abundance in
94 the algal cell was quantified by mass spectrometry as 1.1-1.3 ± 0.3 amol/cell, representing 0.15% of
95 total cell proteins (Hammel, Sommer et al. 2020). In Chlamydomonas protein extracts, SBPase was
96 shown to undergo post-translational modifications by phosphorylation of serines and threonines
97 (Werth, McConnell et al. 2017), and redox modifications of cysteine thiols (Zaffagnini, Bedhomme et
98 al. 2012, Morisse, Zaffagnini et al. 2014, Pérez-Pérez, Mauriès et al. 2017). However, the mechanisms
99 by which post-translational modifications affect the catalytic activity of CrSBPase is still lacking. Here,
100 we describe the crystal structures of *Cr*SBPase in two redox states, examine the catalytic activity of
101 recombinant CrSBPase, and investigate the correlation between the redox state and the

102 oligomerization of the protein. Our results suggest that a redox control over oligomer equilibrium
103 could represent a novel mechanism to regulate enzymatic activities in the CBBC.
104

105 **Material and methods**

106 Chemical reagents were purchased from Merck (Darmstadt, Germany), chromatography material
107 was provided by Cytiva (Vélizy-Villacoublay, France), crystallization solutions and consumable were
108 purchased from Qiagen (Hilden, Germany), Hampton Research (Aliso Viejo, CA USA), and SPT Labtech
109 (Melbourn, UK).
110

111 **Cloning and mutagenesis of *Cr*SBPase expression plasmids**

112 The sequence coding for full-length mature SBPase was amplified by reverse transcriptase
113 polymerase chain reaction (RT-PCR) from *Chlamydomonas reinhardtii* total ribonucleic acids extract
114 and inserted at sites 5'-NdeI and BamHI-3' into expression vector pET3c modified for the fusion of an
115 amino-terminal hexa-histidine tag in the recombinant protein, yielding plasmid pSL-175-His_6-
116 *Cr*SBPase-WT. PCR primers were 5'-TCTCGCCATATGGCCGTTCTGACCCAGGCC-3' (forward, NdeI site
117 underlined) and 5'-CGGGTGGGATCCTTAGGCAGCCACCTTCTC-3' (reverse, BamHI site underlined). The
118 encoded protein encompasses 331 amino acids, with a molar mass of 36,176.7 Da and a theoretical
119 extinction coefficient of 24,722.5 $M^{-1}.cm^{-1}$. Unless otherwise stated, amino acid residues numbering
120 throughout the manuscript is that of GenBank entry DAA79954.1 and Uniprot entries A8IRK4 and
121 P46284. Point mutants of cysteines 115 and 120 singly substituted with serines were generated by
122 site-directed PCR mutagenesis with primers listed in supplementary table 1, producing plasmids pSL-
123 181-His6-*Cr*SBPase-C115S, and pSL-182-His6-*Cr*SBPase-C120S.
124

125 **Recombinant *Cr*SBPase purification**

126 Plasmids pSL-175, -181, and -182 were used to transform *Escherichia coli* BL21(DE3). The
127 transformants were grown at 37 °C in 2YT supplemented with 150 µg/mL ampicillin. When cultures

128 reached an OD_{600} of ~0.6, T7-dependent *Cr*SBPase overexpression was induced by the addition of
129 isopropyl-β-D-thiogalactopyranoside (IPTG) at 0.2 mM for 3 h.
130 Harvested cell pellets were resuspended in 20 mM Tris pH 7.9, 100 mM NaCl (buffer A) and lyzed by
131 1 sec / 1 sec pulsed sonication for 3 min. The soluble fraction of the lysate was separated by 20 min
132 centrifugation at 20,000 *g* and loaded on 2 mL Ni-NTA resin for His-tag mediated affinity
133 chromatography. The resin was washed in four steps with 25 mL buffer A, 25 mL buffer A
134 supplemented with 10, 20, and 30 mM imidazole, and *Cr*SBPase was eluted in three steps with 10 mL
135 buffer A supplemented with 100, 200, and 300 mM imidazole. Pooled eluates containing *Cr*SBPase
136 were loaded on HiLoad Superdex 200 26/600 size-exclusion chromatography column and eluted in
137 buffer A. Protein purity was assessed by electrophoresis on 12% acrylamide gel under denaturing and
138 reducing conditions (supplementary figure 1). Peak fractions were assembled and concentrated by
139 ultrafiltration on Amicon units of MWCO 30,000 Da cut-off. Final concentrations of purified proteins
140 were in the 1-10 mg/ml range as measured by Nanodrop ND-2000 spectrophotometer using an ε_{280}
141 of 24,722.5 $M^{-1}.cm^{-1}$.
142
143 **Western blot**
144 Polyclonal antibodies were generated by immunization of rabbits with pure recombinant *Cr*SBPase
145 (Genecust, Boynes France). Analyzed fractions were separated by denaturing polyacrylamide
146 electrophoresis and transferred to 0.2 µm nitrocellulose membrane for detection with primary
147 antibody subsequently detected by secondary anti-rabbit antibodies coupled to horseradish
148 peroxidase. Detection was done with commercial ECL peroxidase assay (GE Healthcare, Chicago IL
149 USA) with a Chemidoc (Bio-Rad, Hercules CA USA).
150
151 **Crystallization and structure determination**
152 Pure recombinant His6-*Cr*SBPase-WT concentrated at 3-6 mg/mL was tested for crystallization on
153 screens JCSG I-IV in 200 nL sitting drops. Single crystals were obtained and optimized with mother

154 liquor 0.1 M sodium HEPES pH=7.5, 2% (v/v) polyethylene glycol 400, 2.0 M ammonium sulfate, flash-
155 frozen in mother liquor supplemented with 25% glycerol and tested for X-ray diffraction. Complete X-
156 ray diffraction datasets were collected at SOLEIL beamline Proxima-2A and allowed the
157 determination of the crystal structure by model replacement with 5iz3, the structure of ortholog
158 SBPase from the moss *Physcomitrium patens.* Model building in COOT and refinement in the PHENIX
159 software suite yielded structure deposited under PDB ID 7b2o (Emsley, Lohkamp et al. 2010) (Adams,
160 Afonine et al. 2011) (Liebschner, Afonine et al. 2019). After we obtained our experimental structure,
161 the European Bioinformatics Institute (Hinxton, UK) communicated high-accuracy prediction models
162 computed by Deepmind AlphaFold 2 (Jumper, Evans et al. 2021), including a prediction of *Cr*SBPase
163 structure (https://alphafold.ebi.ac.uk/entry/P46284) that matches chain A in 7b2o crystal structure
164 with a root mean square deviation (RMSD) of 0.453 Å. Hence, X-ray crystallography and AlphaFold
165 independently contribute to the proposed structural analysis.
166 In order to obtain the structure of *Cr*SBPase in a reduced state, crystals were grown in the presence
167 of 10 mM of the reducing agent tris-(2-carboxyethyl)phosphine (TCEP) in condition JCSG IV E8/56 0.2
168 M lithium sulfate, 0.1 M Tris pH 7.0, and 1.0 M sodium/potassium tartrate. Crystals were cryo-
169 protected in mother liquor supplemented with 25% ethylene glycol, flash-frozen and tested for X-ray
170 diffraction at SOLEIL beamline Proxima-2A. A complete dataset was collected that allowed the
171 determination of the structure by molecular replacement with 7b2o as a template, resulting in
172 structure 7zuv. Among the eight *Cr*SBPase copies of the asymmetric unit, two had their disulfides
173 absent as a consequence of the TCEP treatment while the others six subunits were essentially
174 identical to untreated structures in entry 7b2o (*i.e.*, fully oxidized form).
175

176 **Enzymatic assays**

177 The catalytic activity of 10-200 nM pure recombinant *Cr*SBPase was spectrophotometrically assayed
178 in buffer A by coupling the hydrolysis of 1 mM FBP into F6P to the reduction of 0.5 mM $NADP^+$ into
179 NADPH through isomerization of F6P into glucose-6-phosphate (G6P) by 0.5 $U.mL^{-1}$ phosphoglucose

180 isomerase (PGI) and the oxidation of G6P into 6-phosphogluconolactone (6PGL) by 0.1-0.5 $U.mL^{-1}$
181 glucose-6-phosphate dehydrogenase (G6PDH). Reporter assay is coupled in a molar ratio
182 FBP:F6P:G6P:6PGL of 1:1:1:1 to the oxidation of one molar equivalent of $NADP^+$ into NADPH that we
183 recorded over 20 minutes by measuring the absorbance at 340 nm using a UVIKON
184 spectrophotometer. Pre-treatments with 0-100 mM reduced dithiothreitol (DTTred), 0-30 mM
185 $MgSO_4$, and 0-15 µM recombinant *Cr*TRX-f2 supplemented with 1 mM DTTred (Lemaire, Tedesco et
186 al. 2018) were carried out for 30 min at room temperature before measuring enzyme activity as
187 described above.
188
189 **Titration of accessible cysteine thiols**
190 Quantification of free reactive cysteines on recombinant CrSBPase was performed with 5,5′-dithio-
191 bis-(2-nitrobenzoic acid) (DTNB, Ellman's reagent) mixed with the purified recombinant protein in a
192 200:1 molar ratio in a 1 mL reaction volume containing 100 mM Tris-HCl, pH 7.9 as described
193 previously (Meloni, Fanti et al. 2024). Reaction of DTNB with solvent-exposed cysteine thiols
194 produces 2-nitro-5-thiobenzoate (TNB^-) that we quantified by monitoring the absorbance at 412 nm
195 and a molar extinction coefficient of TNB^- of 14.15 $mM^{-1}.cm^{-1}$. We calculated the number of free
196 reactive cysteines per *Cr*SBPase monomer by dividing the molar concentration of TNB^- by that of the
197 protein.
198
199 **Molecular dynamics**
200 Molecular dynamics (MD) simulations were performed with the Gromacs package (v2021.4). A dimer
201 of CrSBPase was solvated in a rhombic dodecahedron box with at least 8 Å between the protein
202 atoms and the box edges, which corresponds to ~64000 atoms in total (~18000 water molecules) and
203 a triclinic box of 97x97x68 $Å^3$. The box was neutralized with 18 sodium atoms to make it neutral. The
204 starting conformation was the crystallized structure of oxidized CrSBPase, and we protonated C115
205 and C120 to manually create the reduced state. The protein was described with the Amber14SB force

206 field and water with the TIP3P model. Non-bonding interactions were described with standard
207 parameters: van der Waals interactions had a cut-off of 8 Å, and electrostatic interactions were
208 computed with PME with default parameters with a separation between spaces at 8 Å. Bonds
209 containing a hydrogen atom were restrained with the LINCS algorithm with default parameters. After
210 an energy minimization, the system was equilibrated under the NPT conditions with a δt=1 fs
211 timestep, the velocity-rescale thermostat and the Berendsen barostat. Velocities were generated at
212 100 K and the system was heated up to 300 K in 400 ps before performing 100 ps at 300 K. We then
213 ran simulations of 20 µs under the NPT conditions with a δt=2 fs timestep, the velocity-rescale
214 thermostat and the Parrinello-Rahman barostat.
215
216 **Cultivation of Chlamydomonas for native SBPase analysis**
217 *Chlamydomonas reinhardtii* strain D66 was grown in 50 mL Tris-acetate-phosphate (TAP) medium
218 under 40 $\mu E.m^{-2}.s^{-1}$ continuous light until density reached $5x10^4$ $cell.mL^{-1}$, harvested by 10 min
219 centrifugation at 3,000 g. Cell pellet was resuspended in 100 mM Tris-HCl, pH 7.9, 100 mM NaCl, 5
220 mM L-cystéine, 500 µM NADH, and 1 mM EDTA (buffer L) and lysed by 3 freeze-thaw cycles in liquid
221 nitrogen and water bath. Soluble fraction was separated by 10 min centrifugation at 30,000 *g* and
222 loaded for size-exclusion chromatography on a calibrated Superose 6 16/600 column equilibrated in
223 buffer L. Aliquots of 500 µL elution fractions were analyzed by western blot with primary antibodies
224 raised in rabbits against pure recombinant *Cr*SBPase (Covalab, Bron, France) and secondary anti-
225 rabbit IgG coupled to peroxidase (Sigma-Aldrich reference A9169, Saint Louis, USA) revealed by ECL
226 Prime (GE Healthcare).
227
228 **Small-angle X-ray scattering**
229 Pure recombinant *Cr*SBPase was injected on Agilent HPLC BioSEC-3 300 column in buffer A, in line
230 with the X-ray beam capillary at SOLEIL beamline SWING. *Cr*SBPase was untreated or pre-treated

231 with 10 mM of reducing agent dithiothreitol (DTTred). Diffusion curves were analyzed with ATSAS
232 software to determine the molecular mass and oligomeric state of the protein.
233

234 Results and Discussion

235 Crystal structure of *Cr*SBPase

236 Pure recombinant *Cr*SBPase crystallized in space group $P2_12_12$ and provided a complete X-ray
237 diffraction dataset at a resolution of 3.09 Å. The asymmetric unit is composed of six polypeptide
238 chains packing as three dimers and four water molecules could be modeled. All chains align within a
239 root mean square deviation (RMSD) <0.25 Å and can be considered identical. 309 out of the 331
240 residues were built in the electron density, the unmodelled sequences are in the disordered
241 extensions at the amino- and carboxy-termini of the model. *Cr*SBPase folds into two distinct domains
242 (figure 1A-B). The amino-terminal domain (NTD, residues 73-247) is composed of helices 1, 2, and 3
243 and a mixed β-sheet formed by strands 3-9. The carboxy-terminal domain (CTD, residues 248-383) is
244 composed of helices 4, 5, and 8 and helices 6 and 7 that sandwich a mixed β-sheet formed by strands
245 10-13. α-helices 1-3 pack on the amino-terminal end of the seven-strand sheet, while α-helices 4,5,
246 and 8 pack on the carboxy-terminal end of the four-strand sheet. α-helices 6 and 7 are sandwiched in
247 between the two sheets. *Cr*SBPase chain A aligns with previously reported crystal structure of
248 *Pp*SBPase with an RMSD of 0.478 Å (Gütle et al. 2018 PDB 5iz3) (supplementary figure 5C). This close
249 structural similarity between orthologues indicates common structural properties supporting a
250 conservation of the SBPase function in the evolutionary time separating the microalga
251 Chlamydomonas from the land moss *P. patens*. A short antiparallel β-sheet is constituted of 4-
252 residue strands 1 and 2 separated by a β-turn and preceded by loop A_{113}SCAGTAC_{120}. This motif
253 projects to solvent from α-helices 2 and 3 (figure 1C-D). Residues 113-130 forming the loop and β-
254 hairpin (LBH) motif are positioned away from the core of the protein, at 15.3 Å from water molecule
255 401 (W401), and will be further discussed in the next sections.

256 AF2 entry AF-P46284-F1-model_v4 from AlphaFold Protein Structure Database aligns with our crystal
257 structure 7b2o chain E with RMSD = 0.434 Å, showing excellent agreement between experiment and
258 prediction at the level of protein main chain. Exceptions are in local differences in several loops
259 conformations and in the N-ter and C-ter borders of secondary structure elements. Numerous amino
260 acid residues side chains adopt moderately distinct orientations between the computational model
261 and the experimental structure.
262 AF3 was recently communicated (Abramson, Adler et al. 2024) along with its online prediction server
263 hosted at https://golgi.sandbox.google.com/. *Cr*SBPase model from AF3 align to our crystal structure
264 7B2O chain A with RMSD = 0.441 Å showing again their strong similarity (supplementary figure 5E,F)
265 and with a small discrepancy between AF2 and AF3 models with RMSD = 0.247 Å. The only significant
266 deviations between 7B2O and AF3 are in the orientation of several side chains and notably on the
267 conformation of region 114-131 that contain the LBH motif.
268
269 **CrSBPase catalytic pocket**
270 *Cr*SBPase is structurally similar to its ortholog from the moss *Physcomitrium patens* (RMSD=0.478 Å)
271 (Gutle, Roret et al. 2016). SBPase is a homolog of FBPase, another enzyme involved in the CBBC in
272 photosynthetic organisms and also ubiquitously involved in neoglucogenesis. Cytosolic isoforms of
273 FBPase from non-plant sources have been extensively studied (Moorhead, Hodgson et al. 1994, Lee
274 and Hahn 2003). For instance, the crystal structure of human muscle FBPase complexed with its
275 substrate (FBP) was solved (PDB entry: 5l0a, to be published). We aligned the structure *Cr*SBPase
276 onto this human FBPase:FBP complex from entry 5l0a, confirming their similarity (RMSD = 0.824 Å)
277 with the notable exception of the LBH motif which is absent in FBPase. In a 4-Å distance to FBPase
278 co-crystallized with FBP we aligned 12 residues that are likely available for FBP or SBP binding by
279 *Cr*SBPase (figure 1E): E155, D173, D176, G177, Y287, G289, G290, M291, K317, L318, R319, and E323.
280 These residues are exposed to the solvent in a continuous surface (figure 1F). W401 could be
281 modelled at the center of the putative SBPase catalytic pocket, in the vicinity of E155, D173, D176,

282 R319, and E323, in the catalytic pocket predicted from alignment with human FBPase bound to FBP.
283 W401 specifically is in bonding distance to catalytic residues D178, D181, and E328. W401 is likely to
284 hydrolyze the substrate SBP.
285
286 **Sites of redox post-translational modifications**
287 Ten cysteines could be located in each monomer of *Cr*SBPase (C115, C120, C149, C153, C169, C222,
288 C231, C340, C355, C362). Previous redox-based proteomic studies exploiting Chlamydomonas cells or
289 protein extract established that *Cr*SBPase undergoes redox modifications by thioredoxin-dependent
290 dithiol/disulfide exchange (Lemaire, Guillon et al. 2004, Pérez-Pérez, Mauriès et al. 2017),S-
291 glutathionylation (Zaffagnini, Bedhomme et al. 2012), or S-nitrosylation (Morisse, Zaffagnini et al.
292 2014). While the putative Cys sites for S-glutathionylation are not known, thioredoxin and S-
293 nitrosylation Cys targets were identified as being C222/C231/C355/C362, and C355/C362,
294 respectively. DTNB-based thiol titration on the native purified SBPase indicates that 4.0 ± 0.6
295 cysteines are likely reactive owing to their relative exposure to solvent in a free thiol form. Amino
296 acid residue accessible surface area and accessibility (ASA) calculation is consistent with DTNB
297 titration, with C149, C153, C231, and C355 exposed to the solvent (ASA respective areas: 0.154 Å^2,
298 0.113 Å^2, 0.308 Å^2, and 10.083 Å^2), and the six others either shielded from solvent (C169, C222, C340,
299 and C362) or engaged in a disulfide bridge (C115, C120) (Ahmad, Gromiha et al. 2004). In *Cr*SBPase
300 crystal structure, C222 and C231 are positioned on neighboring strands of the amino-terminal
301 domain, exposing their thiol 3.5 Å away from each other (figure 1G, supplementary figures 2A-B). The
302 formation of an intramolecular disulfide bridge at this cysteines pair is possible if local main chain
303 rearrangements allow a closer contact. C362 thiol is positioned 10.5 Å away from the nearest thiol
304 group of C340. Additionally, C340 and C362 are exposed on an opposite side of the carboxy-terminal
305 β-sheet, disfavoring the formation of an internal disulfide bridge. C355 points its side chain towards
306 C153 and C169 with a thiol-thiol distance of 4.6 Å and 10.1 Å, respectively. Although not observed in
307 our model, a C355-C153/C169 dithiol-disulfide exchange is thus plausible, as described for plant

308 FBPase (Jacquot, Lopez-Jaramillo et al. 1997). Local rearrangements that occur upon FBPase disulfide
309 reduction causes a larger scale relaxation of the active site required to reach maximal catalytic
310 potential (Chiadmi, Navaza et al. 1999) as kinetically characterized for enzymes from *Arabidopsis*
311 *thaliana* (Yoshida and Hisabori 2018) and *Nicotiana benthamiana* (Zimmer, Swart et al. 2021). In
312 Chlamydomonas and Physcomitrium SBPases, the FBPase-type regulatory disulfide is not observed
313 but the SBPase-type C115-C120 bridge is conserved in a nearly identical position in the LBH motif
314 where it may regulate the enzyme by alternative conformational rearrangements. Indeed, the
315 disulfide-bonded cysteines constrain Chlamydomonas SBPase loop A_{113}SCAGTAC_{120} into a compact
316 lasso that could open into a relaxed conformation hypothetically activating catalysis.
317

318 **Sites of post-translational phosphorylations**

319 *Cr*SBPase was reported to be phosphorylated from algae extracts at residues T112, S114, T118, S123,
320 T310, S311, and T313 (Wagner, Gessner et al. 2006, Werth, McConnell et al. 2017, McConnell, Werth
321 et al. 2018). Consistently with the proximity of these residues in two sectors of the sequence
322 (supplementary figure 3), the candidate modification sites are located in two contiguous regions in
323 the three-dimensional structure (figure 1H). T112, S114, T118, and S123 are exposed to the solvent
324 of the amino-terminal domain. The residues belong to or are located nearby the A_{113}SCAGTAC_{120}
325 motif where phosphorylations may cross-signal with redox modifications on C115 and C120. T310,
326 S311, and T313 are located on the other edge of the enzyme, at the solvent exposed tip of the
327 carboxy-terminal domain. Their co-localization at the T_{310}SPT_{313} motif likely facilitates a coordinated
328 phosphorylation of the three residues by the same kinase. Because both groups of potential
329 phospho-sites are located at 17-18 Å from the catalytic pocket (W401 taken as a reference point),
330 there is no straightforward mechanism by which such modifications would exert a control over
331 *Cr*SBPase activity. Analysis of phospho-mimicking mutants along with the identification of the actual
332 kinases/phosphatases couples that control *Cr*SBPase phosphorylation state would allow to
333 comprehend the role of this putative regulatory mechanism.

334

335 ***Cr*SBPase enzymatic activity**

336 Recombinant *Cr*SBPase was assayed for its capacity to catalyze FBP hydrolysis into F6P (Gutle, Roret
337 et al. 2016), a proxy for the hydrolysis of SBP into S7P that we could not test by lack of available
338 substrate and kinetic reporter method. Previous studies demonstrated that plant SBPase requires the
339 cofactor Mg^{2+} and a chemical reductant (DTTred) to be fully activated *in vitro*, reaching a K_M value of
340 0.05 mM and a k_{cat} of 81 sec^{-1} in optimal conditions (Anderson 1974, Woodrow and Walker 1980,
341 Cadet and Meunier 1988). In agreement with this, we found a total absence of activity in the
342 untreated *Cr*SBPase (data not shown), whereas pre-incubation of the enzyme with DTTred and Mg^{2+}
343 resulted in a strong activation, *eg.* a detectable activity at DTT ≥1 mM (figure 2A) and a stark increase
344 in activity at $MgSO_4$ ≥10 mM (figure 2B). By testing different concentrations of $MgSO_4$ (3, 10, 15, and
345 20 mM) and DTTred (1, 10, 25, 50, and 100 mM), we established that 10 mM of DTT and 10 mM
346 $MgSO_4$ are the optimal conditions to attain the maximum specific activity (figure 2A and 2B).
347 Unexpectedly, DTTred concentrations above 10 mM had a dose-dependent inhibitory effect, causing
348 a drastic drop in activity that probably resulted from structural effects leading to denaturation of the
349 enzyme (figure 2A, DTT ≥25 mM). In contrast, we observed no such inhibitory effect in the presence
350 of magnesium at concentrations above 10 mM (figure 2B). Under physiological conditions, the light-
351 dependent redox regulation of plant SBPase is specifically exerted by f-type thioredoxins (Gutle,
352 Roret et al. 2016), which are reduced by the ferredoxin-thioredoxin cascade (Schürmann and
353 Buchanan 1975). The chloroplast TRX-f2 from *Chlamydomonas reinhardtii* was thus tested and
354 validated for its capacity to activate *Cr*SBPase by reduction, with maximal activation reached at TRX-
355 f2 ≥1 µM and no apparent loss of activity at higher TRX-f2 concentrations (figure 2C). The maximum
356 SBPase reported activity, corresponding to 12.15 ± 2.15 µmol(NADPH) min^{-1} $mg(SBPase)^{-1}$, was
357 obtained by pre-incubating the enzyme with 1 µM *Cr*TRX-f2 supplemented with 1 mM DTT and 10
358 mM $MgSO_4$, and maintained even at higher *Cr*TRX-f2 concentrations (*i.e.*, 5 and 10 µM) (figure 2C).
359 *Cr*SBPase specific activity that we report is comparable to that reported for spinach SBPase with FBP

360 as substrate (3.5 µmol min^{-1} mg^{-1} (Seuter, Busch et al. 2002)) and to that reported for another
361 recombinant Chlamydomonas SBPase with SBP as substrate (7.15 ± 0.61 µmol min^{-1} mg^{-1} (Tamoi,
362 Nagaoka et al. 2005)). We hence conclude that our assay faithfully recapitulate the level of *Cr*SBPase
363 hydrolase function in its reduced state.
364
365 **Redox controlled dynamics of *Cr*SBPase**
366 *Cr*SBPase crystallized under reducing treatment (10 mM TCEP). Among the eight subunits in the
367 asymmetric unit, C115-C120 disulfide is absent in two chains (subunits C colored in magenta and
368 subunits E colored in salmon, figure 3D and 3F), while the other six subunits still have the C115-C120
369 disulfide bridge (figure 3B,C,E,G-I). All other cysteines are unaffected by the reducing treatment,
370 consistently with their thiol form in crystal structure of oxidized state. These six subunits present
371 mildly variable conformations of the A_{113}SCAGTAC_{120} lasso conformation similar to the untreated
372 oxidized structure of *Cr*SBPase (figure 3A). Reduction of the C115-C120 disulfide increases local
373 disorder, and the main chain electron density became uninterpretable over a few residues for
374 subunits C (residues 115-118, 124-127), and subunits E (residues 119-127) (supplementary figure 4).
375 Molecular dynamics (MD) simulations of the reduced structure were performed by starting from a
376 dimer of the crystallized oxidized form and forcing C115 and C120 residues to be reduced in the thiol
377 state (-SH). We then ran two independent replicas of 20 µs of MD. In addition, we also ran two
378 independent replicas of 2 µs of MD in the oxidized form. In one of the replicas of the reduced form
379 (MD1), the protein structure barely changed as observed in the SG(C115)/SG(C120) distance that
380 plateaued at ~7 Å, as well as in the RMSD with respect to the starting conformation that stayed
381 around 2 Å (see supplementary figures 8-9 for plots and 12 for images of the structures). However, in
382 the other replica of the reduced form (MD2), significant changes of conformation appeared: the
383 SG(C115)/SG(C120) distance ended up at ~10 Å with peaks at 20 Å and the RMSD values ended up at
384 3.7 and 2.8 Å (supplementary figures 8-9). The difference between MD1 and MD2 is stronger when
385 one focuses on the RMSD of the mobile motif (residues 112 to 131, supplementary figure 10). We

386 observed that after 17 µs of MD all chains adopted an equilibrated conformation and then fluctuated
387 around that conformation (supplementary figure 10); representative structures extracted from MD
388 were thus obtained from a clustering on the time frame (or block) 17-20 µs.
389 The two chains A and B from MD2 adopt a different final conformation (see figure 4A for the overlap
390 with the crystallized oxidized structure and figure 4B for the overlap with the crystallized reduced
391 structure), and we cannot directly conclude on which one is the most stable. Moreover, the residues
392 115 to 128 of each chain from MD1/2 do not overlap well with the crystallized reduced structure
393 which means that neither of the two chains conformations from MD simulations has converged
394 towards the crystallized state. However, we can observe in the reduced crystallized structure that
395 residues 134-148 form an α-helix which is also present in chain B from MD2 whereas this structure is
396 not kept in chain A from MD2 (see green chain on the right of figures 4A-B). In addition, mobile motif
397 from chain B seems to open towards the solvent in a similar way with what was observed for FBPase
398 (Chiadmi, Navaza et al. 1999). Thus, we conclude that chain B from MD2 is more representative of
399 the true reduced conformation than chain A from MD2. If we compare the mobility of chain B from
400 MD2 in the reduced state with one chain in the oxidized state (also chain B from MD2), we can see
401 that the mobile motif is overall more flexible in the reduced state, which is especially true for
402 residues around C120 (residues 118 to 123, supplementary figure 11). We then analyzed the RMSD
403 of residues 112 to 131 from chain B during MD2 (supplementary figure 12): residues 112, 130 and
404 131 barely move which is expected since they belong or are directly connected to the two α-helixes
405 flanking the mobile motif. At ~6 µs of the trajectory almost all other residues (113-129 residues with
406 the sole exception of C120) display an abrupt change of conformation, with a different magnitude
407 though: starting from ~2 Å, the RMSD jumped to 3 Å for some residues (residue 129) and to 15 Å for
408 other residues (residues 125, 126) (supplementary figures 9, 10, and 12). At ~13.5 µs, another
409 change occurs which involves C120 but not all the other residues. Thus, we conclude that the
410 opening of the mobile motif happens in a concerted way and not sequentially residue per residue.
411

412 **Oligomeric states of *Cr*SBPase**

413 Previous studies reported a homodimeric state for SBPase from the moss *Physcomitrella patens*,
414 deduced from the quaternary structure of recombinant protein in the asymmetric unit of the crystal
415 (Gütle, Roret et al. 2016). Size-exclusion chromatography (SEC) profile of *Cr*SBPase is polydisperse
416 with at least three distinct oligomeric states (figure 6A). Notably, we observed that the protein elutes
417 as a main peak of 79 kDa, close to the mass of a homodimer (theoretical mass from monomer
418 sequence: 36,176.7 Da) and consistently with the crystallized state of moss enzyme. Thorough
419 inspection of the elution profile of *Cr*SBPase revealed a peak broadened by a later-eluting shoulder,
420 with the apparent molecular mass of the tailing species at 48 kDa suggesting the presence of a
421 monomeric state of *Cr*SBPase *in vitro*. A third *Cr*SBPase species elutes at an apparent molecular mass
422 of 145 kDa, that fits with a homotetramer. According to the absorbance of each peak and considering
423 that they represent all states of purified and oxidized *Cr*SBPase in solution, we estimate a repartition
424 percentage of species of 10:53:37 for the tetramer:dimer:monomer mixture (total = 100%). Re-
425 injection of the dimer peak fraction over size-exclusion chromatography yielded a similar mixed
426 profile, supporting a dynamic equilibrium over the time of the experiment (>2 h) (data not shown).

427 *Cr*SBPase was crystallized in space groups $P2_12_12$ or $P12_11$ with respectively 6 and 8 protomers in the
428 asymmetric unit. Proteins Interfaces Structures and Assemblies (PISA) analysis reveals that
429 protomers of both crystals pack as homodimers with extensive subunit interface of buried area 4,170
430 $Å^2$ in a similar manner (figure 5A) (Krissinel and Henrick 2007). In the asymmetric unit of *Cr*SBPase
431 crystallized in reducing conditions (7zuv) or within crystallographic neighboring units of *Cr*SBPase in
432 oxidized state (7b2o), *Cr*SBPase further packs into a homotetramer, a dimer of dimers (figure 5B).
433 The apparent molecular mass of SBPase extracted from *Chlamydomonas* cultures cultivated in TAP
434 medium under 40 $\mu E.m^{-2}.s^{-1}$ illumination is comprised between 130 and 40 kDa with the homodimer
435 representing the predominant state as supported by immunoblot analysis (figure 6B).

436 To further investigate the oligomeric dynamics of CrSBPase, we performed small-angle X-ray
437 scattering (SAXS) analysis of purified (untreated) or reduced enzyme *in vitro* which reveals an

438 increase in the protein radius of gyration from 39 to 62 Å upon reduction (supplementary figure 6).
439 This observation implies a change in the oligomeric state of *Cr*SBPase correlating with the redox
440 state. As a matter of fact, purified *Cr*SBPase tends to precipitate into amorphous aggregates that can
441 be turned into droplets of liquid-liquid phase separation by treatment with 10 mM TCEP
442 (supplementary figure 7). Since the LBH redox module is positioned at the homodimer interface
443 (figure 5C), we postulated that the reduction of the C115-C120 disulfide bond and the subsequent
444 local conformation changes depicted by MD affect the oligomer equilibrium of the enzyme. As a
445 matter of fact, we observed that protein mutants C115S or C120S, which are unable to form the
446 C115-C120 disulfide bond, elute in a different oligomer ratio than wild-type CrSBPase (figure 6A).
447 Indeed, we observed a relative accumulation of monomer and tetramer species at the expense of the
448 dimer state in both mutants, as follows with tetramer:dimer:monomer ratio normalized on a scale of
449 100: WT=9:48:43; mutant C115S=42:25:33; mutant C120S=29:17:54. Size-exclusion chromatography
450 suggests that C115-C120 is involved in the stabilization of the dimer. In order to test the hypothetical
451 relevance of this disulfide bridge over catalysis, we assayed *Cr*SBPase-mC115S and *Cr*SBPase-m120S
452 in the conditions described for wild-type enzyme in results section « *Cr*SBPase enzymatic activity »
453 above. Both Cys mutants behaved as wild-type enzyme, *ie.* they responded to DTT/Mg-dependent
454 activation resembling that of the C115-C120 disulfide-containing protein. No activity was detected
455 for native and untreated forms, while specific activities of C115S and C120S mutants upon treatment
456 with DTT and $MgSO_4$ (10 mM for both compounds) were near the specific activity of WT-SBPase
457 (respectively 96% and 107% to the reference, 13.3 ± 2.5 and 14,9 ± 0,9 µmol(NADPH) min^{-1}
458 mg(SBPase)$^{-1}$ for C115S and C120S mutants) (supplementary figure 14). Considering the standard
459 deviation of measured activities, there is no statistically significant difference between WT and
460 mutants in our assays. Based on these data, we can thus conclude that C115-C120 disulfide bond is
461 not the sole thiol-dependent regulatory mechanism involved in the modulation of *Cr*SBPase activity
462 and that the redox dependency of *Cr*SBPase catalysis likely depends on one or several other cysteine

463 pairs. Future studies are required to shed light on the identity of cysteine residues that contribute to
464 *Cr*SBPase catalytic modulation, other than C115 and C120.
465

466 **Conclusions and perspectives**

467 We report the first crystal structure of an SBPase from the microalga *Chlamydomonas reinhardtii*, a
468 model for the molecular and cell biology of plants. SBPase is a photosynthetic enzyme involved in the
469 regeneration phase of the CBBC cycle proved to be target of multiple regulations that we map onto
470 our structural model. The native folding of *Cr*SBPase is highly similar to that of SBPase from the moss
471 *Physcomitrium patens* and to FBPase from chloroplast or cytoplasmic origins. Notwithstanding its
472 propensity to form crystals, recombinant *Cr*SBPase encompasses a range of oligomeric states,
473 dominated by a homodimeric form susceptible to exchange for monomers, tetramers and higher-
474 order assemblies. This oligomer equilibrium is dynamic and correlates with the presence of a
475 disulfide bridge at the vicinity of the monomer-monomer interface, in the SBPase-specific LBH motif.
476 We postulate that the reversible reduction/oxidation of the C115-C120 pair modulates the
477 oligomerization of *Cr*SBPase, through the induction of a local disorder that we observed in the crystal
478 structure of the protein under reducing conditions and that correlates with computations of
479 molecular dynamics.
480 How this oligomeric exchange impacts the actual activity of the enzyme is an open question but
481 should be aligned with previous reports on the allosteric character of the structurally similar FBPase
482 enzyme which follows dimer/tetramer exchanges (Barciszewski, Wisniewski et al. 2016) with a Hill
483 cooperativity coefficient close to 2 representing positive cooperativity in the context of a homodimer
484 (Giudici-Orticoni, Buc et al. 1990). Recent *in vivo* proteome mapping in *Chlamydomonas reinhardtii*
485 localized SBPase in a punctate region surrounding the Rubisco pyrenoid nearby five other CBBC
486 enzymes: phosphoglycerate kinase 1 (PGK), glyceraldehyde-3-phosphate dehydrogenases (GAP1,
487 GAP3), fructose-bisphosphate aldolase (FBA3), ribulose-5-phosphate 3-epimerase (RPE1), and
488 phosphoribulokinase (PRK) (Wang, Patena et al. 2022). Based on our structure-function study on

489 recombinant SBPase, we can speculate that the altered redox state of SBPase may influence the
490 movement to or from the liquid partition of the stroma, where SBPase is metabolically required to
491 provide its contribution to CBBC reactions near other enzymes of the pathway.
492

493 **Tables.**

494 Table 1. Crystallographic data collections and models building statistics.

	7b2o (untreated)	7zuv (partially reduced)
Wavelength (Å)	0.9801	0.9801
Resolution range (Å)	46.62 - 3.095 (3.206 - 3.095)	48.54 - 3.11 (3.221 - 3.11)
Space group	P 2_1 2_1 2	P 1 2_1 1
Unit cell (Å, °)	178.224 183.652 75.196 90 90 90	53.774 163.462 172.765 90 91.939 90
Total reflections	615155 (55989)	376091 (32376)
Unique reflections	45740 (4245)	53456 (5213)
Multiplicity	13.4 (12.9)	7.0 (6.2)
Completeness (%)	99.34 (94.20)	99.65 (97.17)
Mean I/sigma(I)	12.02 (1.72)	8.54 (1.30)
Wilson B-factor (Å^2)	64.82	68.45
R-merge	0.495 (1.877)	0.2492 (1.502)
R-meas	0.5144 (1.954)	0.2691 (1.64)
R-pim	0.1386 (0.5343)	0.1009 (0.6477)
CC1/2	0.983 (0.623)	0.988 (0.479)
CC*	0.996 (0.876)	0.997 (0.805)
Reflections used in refinement	45607 (4242)	53417 (5193)
Reflections used for R-free	1986 (183)	1983 (191)
R-work	0.1942 (0.3071)	0.1963 (0.3239)
R-free	0.2390 (0.3482)	0.2328 (0.3740)
CC(work)	0.944 (0.788)	0.956 (0.726)
CC(free)	0.912 (0.649)	0.949 (0.596)
Number of non-hydrogen atoms	14194	18714
Macromolecules	14190	18704
Solvent	4	10
Protein residues	1859	2451
RMS(bonds) (Å)	0.005	0.004
RMS(angles) (°)	0.75	0.73
Ramachandran favored (%)	94.26	94.80
Ramachandran allowed (%)	5.52	4.70
Ramachandran outliers (%)	0.22	0.50
Rotamer outliers (%)	0.13	0.55
Clashscore	4.88	6.60
Average B-factor (Å^2)	67.00	68.41
macromolecules (Å^2)	67.01	68.40
solvent (Å^2)	49.59	94.37

495 Statistics for the highest-resolution shell are shown in parentheses.

496

497 **Figures legends**

498 **Figure 1. Crystal structure of *Cr*SBPase.**

499 (**A**) Topology is displayed as cartoon with main chain colored from blue (amino-terminus) to red
500 (carboxy-terminus). (**B**) Rotated view of A. by x-axis over -90°. (**C**) Close-up view of region
501 A_{113}SCAGTAC_{120} with disulfide bond shown in sticks. (**D**) Rotated view of C. by x-axis over -90°. (**E**)
502 Putative active site residues inferred from alignment with FBPase bound to FBP (5l0a, human muscle
503 fructose-1,6-bisphosphatase E69Q mutant in active R-state in complex with fructose-1,6-
504 bisphosphate) are represented in sticks. Residue numbering is according to Chlamydomonas SBPase
505 Uniprot entry P46284. (F) Surface representation in the B. orientation with putative active site
506 residues colored in cyan. Water molecule 401 (W401) oxygen is represented as a red sphere. (G)
507 Cysteines site chains are represented in spheres. (H) Threonines and serines side chains reported to
508 be the target of phosphorylations are represented in spheres.

509

510 **Figure 2. Functional characterization of CrSBPase *in vitro*.**

511 Reported enzymatic activity of *Cr*SBPase assayed for (**A**) reduction by reduced dithiothreitol (DTTred)
512 and 10 mM of $MgSO_4$, (**B**) Magnesium sulfate ($MgSO_4$) and 10 mM DTTred, and (**C**) recombinant
513 thioredoxin f2 from *Chlamydomonas reinhardtii* (*Cr*TRX-f2) and 10 mM $MgSO_4$, 1 mM DTT.

514

515 **Figure 3. Crystallographic structures of *Cr*SBPase under reducing treatment: local disorder of the**
516 **A_{113}SCAGTAC_{120} loop.**

517 Main chain was traced according to crystallographic b-factor, with large orange sections representing
518 high b-factor values and thin blue sections representing low b-factors. A-I. Aligned structures of
519 *Cr*SBPase protomers without redox treatment (A, 7b2o chain A) or in the presence of 10 mM TCEP
520 reducing agent (B-I, 7zuv chains A-H).

521

522

523

524 **Figure 4. Molecular dynamics simulation of *Cr*SBPase after reduction.**

525 (**A**) Overlap of the crystallographic structure of oxidized *Cr*SBPase and representative structures of
526 equilibrated reduced *Cr*SBPase during molecular dynamics simulation 2 (MD2). For structures
527 extracted from MD, only residues 109 to 148 are displayed since most of the other residues are
528 closely overlapping those of the crystallographic structure. (**B**) Overlap of the crystallographic
529 structure of reduced *Cr*SBPase and representative structures of equilibrated reduced *Cr*SBPase
530 during MD2. For structures extracted from MD, only residues 109 to 148 are displayed.

531

532 **Figure 5. Oligomeric state of *Cr*SBPase in the crystal.**

533 (**A**) Asymmetric unit dimer of untreated *Cr*SBPase (7b2o). Chains are represented in cartoon and
534 colored cyan (chain B) and salmon (chain E). (**B**) Asymmetric unit homotetramer under reducing
535 treatment (7zuv). Chains A (cyan), C (magenta), F (white), and H (orange) belong to the same
536 asymmetric unit. (**C**) Close-up view on figure A homodimer interface. Loop 113-ASCAGTAC-120 from
537 chain B (in cyan) is in 5-Å distance of neighboring chain E (in salmon). C115 and C120 are bonded by a
538 disulfide bridge.

539

540 **Figure 6. Oligomeric state of *Cr*SBPase *in vitro*.**

541 (**A**) Size-exclusion chromatograms of *Cr*SBPase wild-type (blue), mutant C115S (orange), mutant
542 C120S (gray) on Superdex 200 26/600 GL column. (**B**) Size-exclusion fractionation of Chlamydomonas
543 cell extracts. Chlamydomonas cell culture was harvested, lysed and the soluble fraction of the lysate
544 was loaded on Superose6 16/600 size-exclusion column. Chromatography fractions were analyzed by
545 western blot with anti-*Cr*SBPase primary antibodies. First membrane was loaded with fractions
546 eluted from 40 to 80 mL. Second membrane was loaded with fractions eluted from 80 to 120 mL. M
547 lane is loaded with molecular mass standards ladder. Recombinant CrSBPase was loaded was loaded
548 on the last lane to the right..

549

550 ## Supplementary information

551 **Supplementary table 1. Primers used for point mutagenesis.**

5'-forward C115S	CCGCACCGCCTCGAGCGCCGGTACCGCCTGCGTG
3'-reverse C115S	CACGCAGGCGGTACCGGCGCTCGAGGCGGTGCGG
5'-forward C120S	GCGCCGGTACCGCCAGCGTGAACAGCTTCGGCG
3'-reverse C120S	CGCCGAAGCTGTTCACGCTGGCGGTACCGGCGC

552

553 **Supplementary figure 1. Purification of recombinant *Cr*SBPase.**

554 A. Size-exclusion chromatography profile recorded at absorbance λ= 280 nm on Superdex 200 26/600
555 GL column. B. Electrophoresis of affinity-chromatography fractions on 12% acrylamide gel in
556 denaturing and reducing condition. Gel was stained with Coomassie blue. Mw: molecular mass
557 standards ladder.

558

559 **Supplementary figure 2. Cysteines pair C222-C231 close-up view.**

560 *Cr*SBPase structure 7b2o zoomed around the pair of cysteines 222 and 231 suggests they may form a
561 reversible disulfide bridge, with a thiol-to-thiol distance of 3.5 Å.

562

563 **Supplementary figure 3. SBPase multiple sequences alignment.**

564 *Cr*SBPase mature sequence was used for a BLAST search. Retrieved homolog sequences were aligned
565 and colored-coded according to residue conservation. Illustration made with EndScript (Robert and
566 Gouet 2014).

567

568 **Supplementary figure 4. Related to figure 3. Crystallographic structures of *Cr*SBPase under reducing**
569 **treatment: local main chain rearrangement and variety of cysteine states of the A_{113}SCAGTAC_{120}**
570 **loop.**
571
572
573 **Supplementary figure 5. Structure, oligomerisation and sequence variations according to X-ray**
574 **crystallography and AlphaFold predictions.**
575 A. Surface representation of 7b2o homodimer, colored according to ConSurf (Glaser, Pupko et al.
576 2003) conservation score from teal (lowest conservation) to purple (highest conservation) among
577 150 aligned homologs. B. Hybrid cartoon and surface representation, colored according to ConSurf.
578 C. Superimposition of the crystal structure of *Pp*SBPase (5iz3) (Gütle, Roret et al. 2016) and *Cr*SBPase
579 (7b2o, this study). D. Close-up view on redox motif on superimposed SBPases. E-H. Aligned chain A
580 from 7b2o crystal structure and predicted monomer/dimer/tetramer according to AlphaFold3. Color
581 code of AF3 models is according to plDDT: navy blue very high plDDT>0.9; cyan confident
582 90>plDDT>70; yellow low 70>plDDT>50; orange very low plDDT<50.
583
584 **Supplementary figure 6. Size-exclusion chromatography coupled to small angle X-rays scattering**
585 **(SEC-SAXS) of *Cr*SBPase.**
586 A. X-ray scattering curve log(I) = f(s) for pure *Cr*SBPase untreated (dark blue) or treated (light blue)
587 with 10 mM reduced dithiothreitol (DTTred). B. Radius of gyration of untreated protein was
588 computed by ATSAS Primus Guinier Wizard as Rg = 39.14 ± 0.06 Å (Franke, Petoukhov et al. 2017). C.
589 Radius of gyration of DTT-treated protein was computed as Rg = 62.47 ± 0.38 Å.
590
591 **Supplementary figure 7. Phase separation of reduced *Cr*SBPase precipitates.**
592 *Cr*SBPase at 2 mg/mL formed amorphous precipitates after storage at 4 °C for a week. The
593 suspension was sedimented by centrifugation at 20,000 *g* for 20 minutes and a microliter drop of the

594 supernatant or of the pellet were treated with 10 mM TCEP and visualized by binocular optical
595 microscope. A. Untreated precipitate. B. TCEP-treated precipitate. C. Untreated supernatant. D.
596 TCEP-treated supernatant.
597
598 **Supplementary figures 8-12. Computational detail of molecular dynamic simulation.**
599
600 **Supplementary figure 8.**
601 SG(Cys115)/SG(Cys120) distances along the MD trajectories for each chain (left: oxidized state, right:
602 reduced state). Light colors: raw data saved every 100 ps, dark colors: moving average on 20ns blocs.
603
604 **Supplementary figure 9.**
605 RMSD of main chain along the MD trajectories for each chain (left: oxidized state, right: reduced
606 state). Light colors: raw data saved every 100 ps, dark colors: moving average on 20 ns blocs.
607
608 **Supplementary figure 10.**
609 RMSD of main chain of the mobile motif in the reduced state (residues 112 to 131) along the MD
610 trajectories for each chain (left: RMSD with respect to the starting conformation of MD, right: RMSD
611 with respect to the conformation at 20 µs). Light colors: raw data saved every 100 ps, dark colors:
612 moving average on 20 ns blocs.
613
614 **Supplementary figure 11.**
615 RMSF per residue for each chain (top row: full sequence, bottom row: zoom on residues 110 to 170;
616 left column: oxidized state, middle column: reduced state, right column: comparison of one chain
617 from each state).
618

619 **Supplementary figure 12.**

620 RMSD of main chain of each residue from the mobile motif along the trajectory of chain B from MD2.

621 Data are moving average on 200 ns blocs.

622

623 **Supplementary figure 13. Structures of *Cr*SBPase retrieved from molecular dynamics simulations 1**

624 **and 2**.

625 Two independent replicas of 20 µs were performed. In one of them (MD1), the overall structure of

626 both chains of the enzyme barely changed. To illustrate this, we present in supplementary figure 12

627 the overlap between the crystallographic oxidized structure and representative structures extracted

628 from MD (based on clustering the last 3 µs since each chain does not display significative changes

629 after 17 µs). A. Overlap of the crystallographic structure of oxidized *Cr*SBPase and representative

630 structures of equilibrated reduced SBPase during MD1. For structures extracted from MD, only

631 residues 111 to 132 are displayed since the other residues are closely overlapping those of the

632 crystallographic structure. B. Overlap of the crystallographic structure of oxidized SBPase and

633 representative structures of equilibrated reduced *Cr*SBPase during MD2. For structures extracted

634 from MD, only residues 109 to 148 are displayed since most of the other residues are closely

635 overlapping those of the crystallographic structure.

636

637 **Supplementary figure 14.** Regulatory properties of CrSBPase activity.

638 Specific activities of wild-type form (wt) and cysteine mutants (C115S and C120S) were evaluated by

639 treating each *Cr*SBPase form without DTT and Mg^{2+} (/), with only Mg^{2+} (Mg), or with both DTT and

640 Mg^{2+} (DTT + Mg). Specific activities are reported as µmol(NADPH) min^{-1} mg(SBPase)$^{-1}$.

641

642 **Supplementary movie 1. Molecular dynamics simulation of *Cr*SBPase 7B2O chain A upon C115-120**

643 **disulfide bridge reduction.**

644

645 **Supplementary movie 2. Molecular dynamics simulation of *Cr*SBPase 7B2O chain B upon C115-120**
646 **bridge reduction.**
647
648

649 ## Authors contributions

650 JH, NC: Conceptualization; JH, NC, MS, TLM: Data curation; JH, NC, MZ: Formal analysis; JH: Funding
651 acquisition; JH, NC, MZ, SDL, MS, TLM: Investigation; JH, NC, MZ, MS, TLM: Methodology; JH, SDL:
652 Project administration; JH, NC, SDL: Resources; NC: Software; JH, MZ: Supervision; JH, NC, MZ, SDL,
653 MS, TLM: Writing - original draft; JH, NC, MZ, SDL, MS, TLM: Writing - review & editing.
654

655 ## Acknowledgements

656 We acknowledge the Institut de Biologie Physico-Chimique (CNRS, FR 505) for access to the
657 crystallization facility. We acknowledge SOLEIL for provision of synchrotron radiation facilities at
658 beamlines SWING, PROXIMA-1, and PROXIMA-2A. We thank Guillaume Q. Robert for his contribution
659 to protein purification, crystallization under reducing treatment, and model building. Plasmids pSL-
660 175, -181, and -182 were cloned by Dr. Laure Michelet. This work was funded by the grant
661 CALVINTERACT from the Agence Nationale de la Recherche (ANR-19-CE11-0009). Martina Santoni
662 received funding from the University of Bologna and Sorbonne University exchange program
663 ERASMUS+. This work was performed using HPC resources from GENCI–IDRIS (Grant 2021-077156).
664 The authors express their gratitude to the financial support of the CNRS-INSB through a grant «Accès
665 aux infrastructures nationales».
666

667 ## Conflicts of interest statement

668 The authors report no conflict of interest relevant to the conduct or report of this research.
669
670

Bibliography

Abramson, J., J. Adler, J. Dunger, R. Evans, T. Green, A. Pritzel, O. Ronneberger, L. Willmore, A. J. Ballard, J. Bambrick, S. W. Bodenstein, D. A. Evans, C.-C. Hung, M. O'Neill, D. Reiman, K. Tunyasuvunakool, Z. Wu, A. Žemgulytė, E. Arvaniti, C. Beattie, O. Bertolli, A. Bridgland, A. Cherepanov, M. Congreve, A. I. Cowen-Rivers, A. Cowie, M. Figurnov, F. B. Fuchs, H. Gladman, R. Jain, Y. A. Khan, C. M. R. Low, K. Perlin, A. Potapenko, P. Savy, S. Singh, A. Stecula, A. Thillaisundaram, C. Tong, S. Yakneen, E. D. Zhong, M. Zielinski, A. Žídek, V. Bapst, P. Kohli, M. Jaderberg, D. Hassabis and J. M. Jumper (2024). "Accurate structure prediction of biomolecular interactions with AlphaFold 3." Nature.

Adams, P. D., P. V. Afonine, G. Bunkóczi, V. B. Chen, N. Echols, J. J. Headd, L. W. Hung, S. Jain, G. J. Kapral, R. W. Grosse Kunstleve, A. J. McCoy, N. W. Moriarty, R. D. Oeffner, R. J. Read, D. C. Richardson, J. S. Richardson, T. C. Terwilliger and P. H. Zwart (2011). "The Phenix software for automated determination of macromolecular structures." Methods **55**(1): 94-106.

Ahmad, S., M. Gromiha, H. Fawareh and A. Sarai (2004). "ASAView: database and tool for solvent accessibility representation in proteins." BMC Bioinformatics **5**: 51.

Almagro Armenteros, J. J., M. Salvatore, O. Emanuelsson, O. Winther, G. von Heijne, A. Elofsson and H. Nielsen (2019). "Detecting sequence signals in targeting peptides using deep learning." Life Sci Alliance **2**(5).

Anderson, L. E. (1974). "Activation of pea leaf chloroplast sedoheptulose 1,7-diphosphate phosphatase by light and dithiothreitol." Biochem Biophys Res Commun **59**(3): 907-913.

Barciszewski, J., J. Wisniewski, R. Kolodziejczyk, M. Jaskolski, D. Rakus and A. Dzugaj (2016). "T-to-R switch of muscle fructose-1,6-bisphosphatase involves fundamental changes of secondary and quaternary structure." Acta Crystallogr D Struct Biol **72**(Pt 4): 536-550.

Cadet, F. and J. C. Meunier (1988). "pH and kinetic studies of chloroplast sedoheptulose-1,7-bisphosphatase from spinach (Spinacia oleracea)." Biochem J **253**(1): 249-254.

Calvin, M. (1962). "The path of carbon in photosynthesis." Science **135**(3507): 879-889.

Chiadmi, M., A. Navaza, M. Miginiac-Maslow, J. P. Jacquot and J. Cherfils (1999). "Redox signalling in the chloroplast: structure of oxidized pea fructose-1,6-bisphosphate phosphatase." Embo j **18**(23): 6809-6815.

Cotton, C. A., B. V. Kabasakal, N. A. Miah and J. W. Murray (2015). "Structure of the dual-function fructose-1,6/sedoheptulose-1,7-bisphosphatase from Thermosynechococcus elongatus bound with sedoheptulose-7-phosphate." Acta Crystallogr F Struct Biol Commun **71**(Pt 10): 1341-1345.

Emanuelsson, O., S. Brunak, G. von Heijne and H. Nielsen (2007). "Locating proteins in the cell using TargetP, SignalP and related tools." Nat Protoc **2**(4): 953-971.

Emsley, P., B. Lohkamp, W. G. Scott and K. Cowtan (2010). "Features and development of Coot." Acta Crystallogr D Biol Crystallogr **66**(Pt 4): 486-501.

Feng, L., Y. Han, G. Liu, B. An, J. Yang, G. Yang, Y. Li and Y. Zhu (2007). "Overexpression of sedoheptulose-1,7-bisphosphatase enhances photosynthesis and growth under salt stress in transgenic rice plants." Funct Plant Biol **34**(9): 822-834.

Feng, L., K. Wang, Y. Li, Y. Tan, J. Kong, H. Li, Y. Li and Y. Zhu (2007). "Overexpression of SBPase enhances photosynthesis against high temperature stress in transgenic rice plants." Plant Cell Rep **26**(9): 1635-1646.

Franke, D., M. V. Petoukhov, P. V. Konarev, A. Panjkovich, A. Tuukkanen, H. D. T. Mertens, A. G. Kikhney, N. R. Hajizadeh, J. M. Franklin, C. M. Jeffries and D. I. Svergun (2017). "ATSAS 2.8: a comprehensive data analysis suite for small-angle scattering from macromolecular solutions." J Appl Crystallogr **50**(Pt 4): 1212-1225.

Giudici-Orticoni, M. T., J. Buc, M. Bidaud and J. Ricard (1990). "Thermodynamics of information transfer between subunits in oligomeric enzymes and kinetic cooperativity. 3. Information transfer between the subunits of chloroplast fructose bisphosphatase." Eur J Biochem **194**(2): 483-490.

720 Glaser, F., T. Pupko, I. Paz, R. E. Bell, D. Bechor-Shental, E. Martz and N. Ben-Tal (2003). "ConSurf:
721 identification of functional regions in proteins by surface-mapping of phylogenetic information."
722 Bioinformatics **19**(1): 163-164.
723 Gutle, D. D., T. Roret, S. J. Muller, J. Couturier, S. D. Lemaire, A. Hecker, T. Dhalleine, B. B. Buchanan,
724 R. Reski, O. Einsle and J. P. Jacquot (2016). "Chloroplast FBPase and SBPase are thioredoxin-linked
725 enzymes with similar architecture but different evolutionary histories." Proc Natl Acad Sci U S A
726 **113**(24): 6779-6784.
727 Gütle, D. D., T. Roret, S. J. Müller, J. Couturier, S. D. Lemaire, A. Hecker, T. Dhalleine, B. B. Buchanan,
728 R. Reski, O. Einsle and J. P. Jacquot (2016). "Chloroplast FBPase and SBPase are thioredoxin-linked
729 enzymes with similar architecture but different evolutionary histories." Proc Natl Acad Sci U S A
730 **113**(24): 6779-6784.
731 Hammel, A., F. Sommer, D. Zimmer, M. Stitt, T. Mühlhaus and M. Schroda (2020). "Overexpression of
732 Sedoheptulose-1,7-Bisphosphatase Enhances Photosynthesis in Chlamydomonas reinhardtii and Has
733 No Effect on the Abundance of Other Calvin-Benson Cycle Enzymes." Front Plant Sci **11**: 868.
734 Jacquot, J. P., J. Lopez-Jaramillo, M. Miginiac-Maslow, S. Lemaire, J. Cherfils, A. Chueca and J. Lopez-
735 Gorge (1997). "Cysteine-153 is required for redox regulation of pea chloroplast fructose-1,6-
736 bisphosphatase." FEBS Lett **401**(2-3): 143-147.
737 Johnson, M. P. (2016). "Photosynthesis." Essays Biochem **60**(3): 255-273.
738 Johnson, X. and J. Alric (2013). "Central carbon metabolism and electron transport in
739 Chlamydomonas reinhardtii: metabolic constraints for carbon partitioning between oil and starch."
740 Eukaryot Cell **12**(6): 776-793.
741 Jumper, J., R. Evans, A. Pritzel, T. Green, M. Figurnov, O. Ronneberger, K. Tunyasuvunakool, R. Bates,
742 A. Zidek, A. Potapenko, A. Bridgland, C. Meyer, S. A. A. Kohl, A. J. Ballard, A. Cowie, B. Romera-
743 Paredes, S. Nikolov, R. Jain, J. Adler, T. Back, S. Petersen, D. Reiman, E. Clancy, M. Zielinski, M.
744 Steinegger, M. Pacholska, T. Berghammer, S. Bodenstein, D. Silver, O. Vinyals, A. W. Senior, K.
745 Kavukcuoglu, P. Kohli and D. Hassabis (2021). "Highly accurate protein structure prediction with
746 AlphaFold." Nature **596**(7873): 583-589.
747 Krissinel, E. and K. Henrick (2007). "Inference of macromolecular assemblies from crystalline state." J
748 Mol Biol **372**(3): 774-797.
749 Kubis, A. and A. Bar-Even (2019). "Synthetic biology approaches for improving photosynthesis." J Exp
750 Bot **70**(5): 1425-1433.
751 Lee, S. W. and T. R. Hahn (2003). "Light-regulated differential expression of pea chloroplast and
752 cytosolic fructose-1,6-bisphosphatases." Plant Cell Rep **21**(6): 611-618.
753 Lefebvre, S., T. Lawson, O. V. Zakhleniuk, J. C. Lloyd, C. A. Raines and M. Fryer (2005). "Increased
754 sedoheptulose-1,7-bisphosphatase activity in transgenic tobacco plants stimulates photosynthesis
755 and growth from an early stage in development." Plant Physiol **138**(1): 451-460.
756 Lemaire, S. D., B. Guillon, P. Le Maréchal, E. Keryer, M. Miginiac-Maslow and P. Decottignies (2004).
757 "New thioredoxin targets in the unicellular photosynthetic eukaryote *Chlamydomonas reinhardtii*."
758 Proc Natl Acad Sci U S A **101**(19): 7475-7480.
759 Lemaire, S. D., D. Tedesco, P. Crozet, L. Michelet, S. Fermani, M. Zaffagnini and J. Henri (2018).
760 "Crystal Structure of Chloroplastic Thioredoxin f2 from Chlamydomonas reinhardtii Reveals Distinct
761 Surface Properties." Antioxidants (Basel) **7**(12).
762 Liebschner, D., P. V. Afonine, M. L. Baker, G. Bunkóczi, V. B. Chen, T. I. Croll, B. Hintze, L. W. Hung, S.
763 Jain, A. J. McCoy, N. W. Moriarty, R. D. Oeffner, B. K. Poon, M. G. Prisant, R. J. Read, J. S. Richardson,
764 D. C. Richardson, M. D. Sammito, O. V. Sobolev, D. H. Stockwell, T. C. Terwilliger, A. G. Urzhumtsev, L.
765 L. Videau, C. J. Williams and P. D. Adams (2019). "Macromolecular structure determination using X-
766 rays, neutrons and electrons: recent developments in Phenix." Acta Crystallogr D Struct Biol **75**(Pt
767 10): 861-877.
768 McConnell, E. W., E. G. Werth and L. M. Hicks (2018). "The phosphorylated redox proteome of
769 Chlamydomonas reinhardtii: Revealing novel means for regulation of protein structure and function."
770 Redox Biol **17**: 35-46.

771 Meloni, M., S. Fanti, D. Tedesco, L. Gurrieri, P. Trost, S. Fermani, S. D. Lemaire, M. Zaffagnini and J.
772 Henri (2024). "Characterization of chloroplast ribulose-5-phosphate-3-epimerase from the microalga
773 Chlamydomonas reinhardtii." Plant Physiol **194**(4): 2263-2277.
774 Mettler, T., T. Muhlhaus, D. Hemme, M. A. Schottler, J. Rupprecht, A. Idoine, D. Veyel, S. K. Pal, L.
775 Yaneva-Roder, F. V. Winck, F. Sommer, D. Vosloh, B. Seiwert, A. Erban, A. Burgos, S. Arvidsson, S.
776 Schonfelder, A. Arnold, M. Gunther, U. Krause, M. Lohse, J. Kopka, Z. Nikoloski, B. Mueller-Roeber, L.
777 Willmitzer, R. Bock, M. Schroda and M. Stitt (2014). "Systems Analysis of the Response of
778 Photosynthesis, Metabolism, and Growth to an Increase in Irradiance in the Photosynthetic Model
779 Organism Chlamydomonas reinhardtii." Plant Cell **26**(6): 2310-2350.
780 Moorhead, G. B., R. J. Hodgson and W. C. Plaxton (1994). "Copurification of cytosolic fructose-1,6-
781 bisphosphatase and cytosolic aldolase from endosperm of germinating castor oil seeds." Arch
782 Biochem Biophys **312**(2): 326-335.
783 Morisse, S., M. Zaffagnini, X. H. Gao, S. D. Lemaire and C. H. Marchand (2014). "Insight into protein S-
784 nitrosylation in Chlamydomonas reinhardtii." Antioxid Redox Signal **21**(9): 1271-1284.
785 Nishizawa, A. N. and B. B. Buchanan (1981). "Enzyme regulation in C4 photosynthesis. Purification
786 and properties of thioredoxin-linked fructose bisphosphatase and sedoheptulose bisphosphatase
787 from corn leaves." J Biol Chem **256**(12): 6119-6126.
788 Ohta, J. (2022). "A novel variant of the Calvin-Benson cycle bypassing fructose bisphosphate." Sci Rep
789 **12**(1): 3984.
790 Pérez-Pérez, M. E., A. Mauriès, A. Maes, N. J. Tourasse, M. Hamon, S. D. Lemaire and C. H. Marchand
791 (2017). "The Deep Thioredoxome in Chlamydomonas reinhardtii: New Insights into Redox
792 Regulation." Mol Plant **10**(8): 1107-1125.
793 Raines, C. A. (2022). "Improving plant productivity by re-tuning the regeneration of RuBP in the
794 Calvin-Benson-Bassham cycle." New Phytol **236**(2): 350-356.
795 Robert, X. and P. Gouet (2014). "Deciphering key features in protein structures with the new
796 ENDscript server." Nucleic Acids Research **42**(W1): W320-W324.
797 Rosenthal, D. M., A. M. Locke, M. Khozaei, C. A. Raines, S. P. Long and D. R. Ort (2011). "Over-
798 expressing the C(3) photosynthesis cycle enzyme Sedoheptulose-1-7 Bisphosphatase improves
799 photosynthetic carbon gain and yield under fully open air CO(2) fumigation (FACE)." BMC Plant Biol
800 **11**: 123.
801 Schmollinger, S., T. Mühlhaus, N. R. Boyle, I. K. Blaby, D. Casero, T. Mettler, J. L. Moseley, J. Kropat, F.
802 Sommer, D. Strenkert, D. Hemme, M. Pellegrini, A. R. Grossman, M. Stitt, M. Schroda and S. S.
803 Merchant (2014). "Nitrogen-Sparing Mechanisms in Chlamydomonas Affect the Transcriptome, the
804 Proteome, and Photosynthetic Metabolism." Plant Cell **26**(4): 1410-1435.
805 Schürmann, P. and B. B. Buchanan (1975). "Role of ferredoxin in the activation of sedoheptulose
806 diphosphatase in isolated chloroplasts." Biochim Biophys Acta **376**(1): 189-192.
807 Seuter, A., M. Busch and R. Hain (2002). "Overexpression of the potential herbicide target
808 sedoheptulose-1,7-bisphosphatase from Spinacia oleracea in transgenic tobacco." Molecular
809 Breeding **9**(1): 53-61.
810 Simkin, A. J., P. E. Lopez-Calcagno, P. A. Davey, L. R. Headland, T. Lawson, S. Timm, H. Bauwe and C.
811 A. Raines (2017). "Simultaneous stimulation of sedoheptulose 1,7-bisphosphatase, fructose 1,6-
812 bisphophate aldolase and the photorespiratory glycine decarboxylase-H protein increases CO(2)
813 assimilation, vegetative biomass and seed yield in Arabidopsis." Plant Biotechnol J **15**(7): 805-816.
814 Tamoi, M., M. Nagaoka and S. Shigeoka (2005). "Immunological properties of sedoheptulose-1,7-
815 bisphosphatase from Chlamydomonas sp. W80." Biosci Biotechnol Biochem **69**(4): 848-851.
816 Wagner, V., G. Gessner, I. Heiland, M. Kaminski, S. Hawat, K. Scheffler and M. Mittag (2006).
817 "Analysis of the phosphoproteome of Chlamydomonas reinhardtii provides new insights into various
818 cellular pathways." Eukaryot Cell **5**(3): 457-468.
819 Wang, L., W. Patena, K. A. Van Baalen, Y. Xie, E. R. Singer, S. Gavrilenko, M. Warren-Williams, L. Han,
820 H. R. Harrigan, V. Chen, V. T. N. P. Ton, S. Kyin, H. H. Shwe, M. H. Cahn, A. T. Wilson, J. Hu, D. J.
821 Schnell, C. D. McWhite and M. Jonikas (2022). "A Chloroplast Protein Atlas Reveals Novel Structures
822 and Spatial Organization of Biosynthetic Pathways." bioRxiv: 2022.2005.2031.493820.

823 Werth, E. G., E. W. McConnell, T. S. Gilbert, I. Couso Lianez, C. A. Perez, C. K. Manley, L. M. Graves, J.
824 G. Umen and L. M. Hicks (2017). "Probing the global kinome and phosphoproteome in
825 Chlamydomonas reinhardtii via sequential enrichment and quantitative proteomics." Plant J **89**(2):
826 416-426.
827 Woodrow, I. E. (1982). "Sedoheptulose-1,7-bisphosphatase from wheat chloroplasts." Methods
828 Enzymol **90 Pt E**: 392-396.
829 Woodrow, I. E. and D. A. Walker (1980). "Light-mediated activation of stromal sedoheptulose
830 bisphosphatase." Biochem J **191**(3): 845-849.
831 Yoshida, K. and T. Hisabori (2018). "Determining the Rate-Limiting Step for Light-Responsive Redox
832 Regulation in Chloroplasts." Antioxidants (Basel) **7**(11).
833 Zaffagnini, M., M. Bedhomme, C. H. Marchand, S. Morisse, P. Trost and S. D. Lemaire (2012). "Redox
834 regulation in photosynthetic organisms: focus on glutathionylation." Antioxid Redox Signal **16**(6):
835 567-586.
836 Zimmer, D., C. Swart, A. Graf, S. Arrivault, M. Tillich, S. Proost, Z. Nikoloski, M. Stitt, R. Bock, T.
837 Mühlhaus and A. Boulouis (2021). "Topology of the redox network during induction of
838 photosynthesis as revealed by time-resolved proteomics in tobacco." Sci Adv **7**(51): eabi8307.
839

Figure 1.

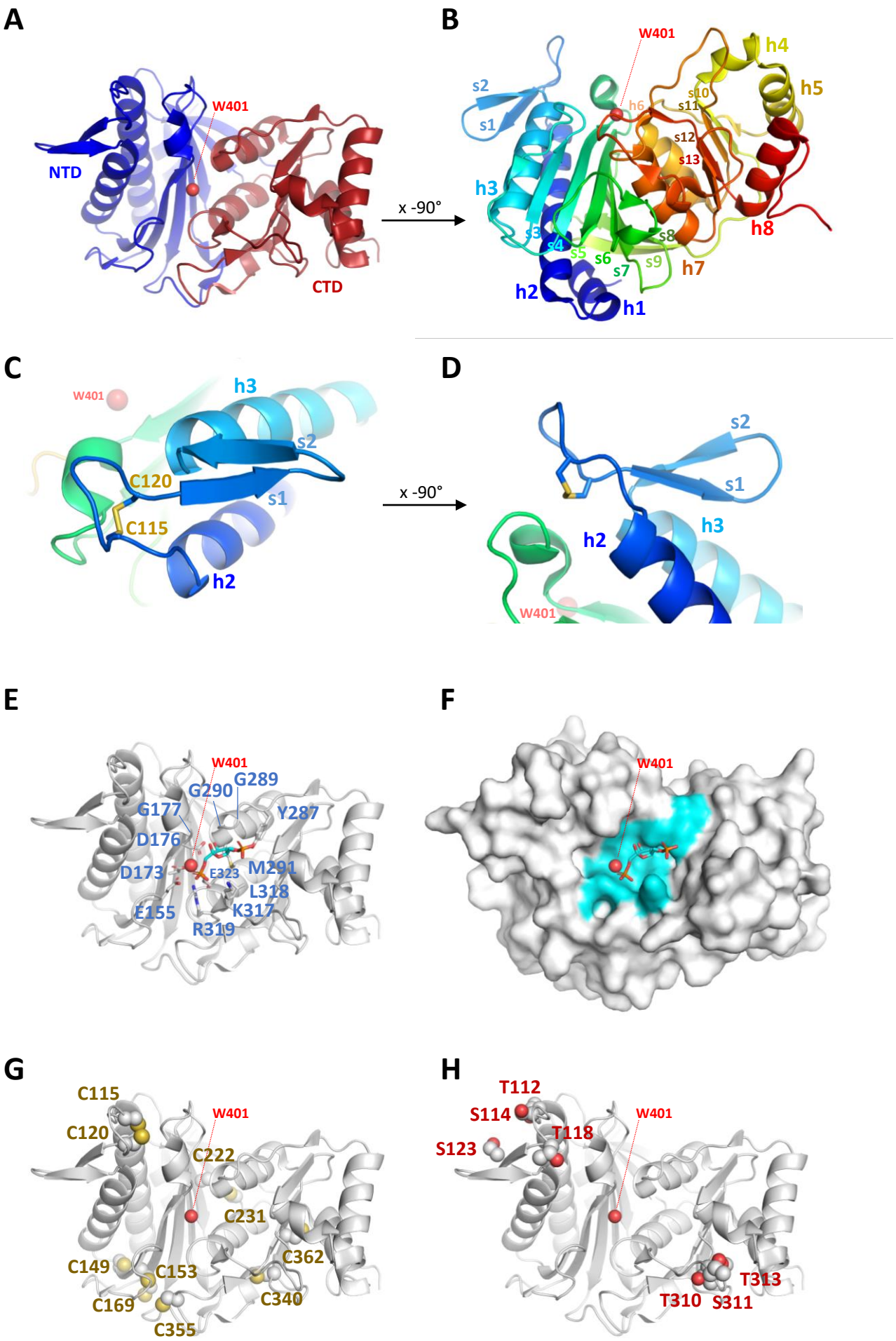
A
W401
NTD
CTD
x -90°
B
W401
h4
h5
s2
s1
h6
s10
s11
s12
s13
h3
s3
s4
s5
s6
s7
s8
s9
h7
h8
h2
h1
C
W401
h3
s2
C120
s1
C115
h2
x -90°
D
s2
s1
h3
h2
W401
E
W401
G289
G290
G177
Y287
D176
D173
E323
M291
L318
E155
K317
R319
F
W401
G
C115
C120
W401
C222
C231
C149
C153
C362
C169
C340
C355
H
T112
S114
W401
T118
S123
T313
T310
S311

Figure 2.

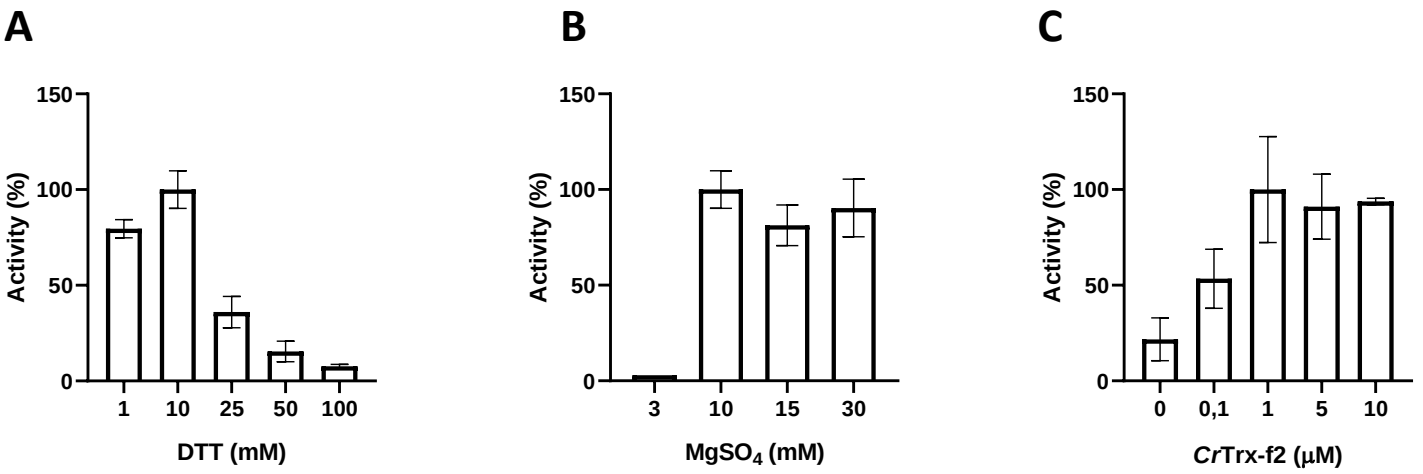
A
B
C
150
100
50
0
Activity (%)
1
10
25
50
100
DTT (mM)
3
10
15
30
MgSO4 (mM)
0
0,1
1
5
10
CrTrx-f2 (µM)

Figure 3.

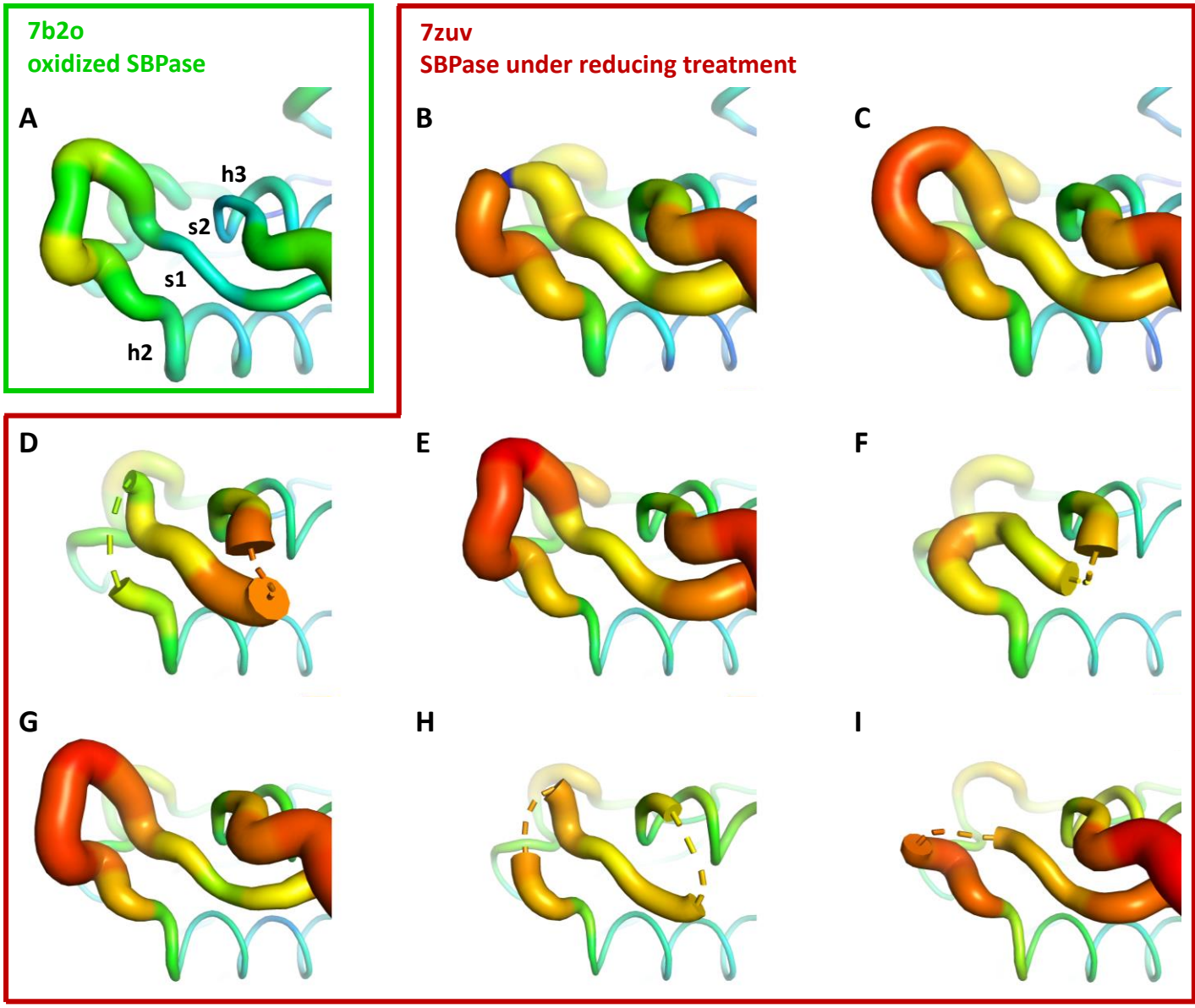
7b2o
oxidized SBPase
A
h3
s2
s1
h2
7zuv
SBPase under reducing treatment
B
C
D
E
F
G
H
I

Figure 4.

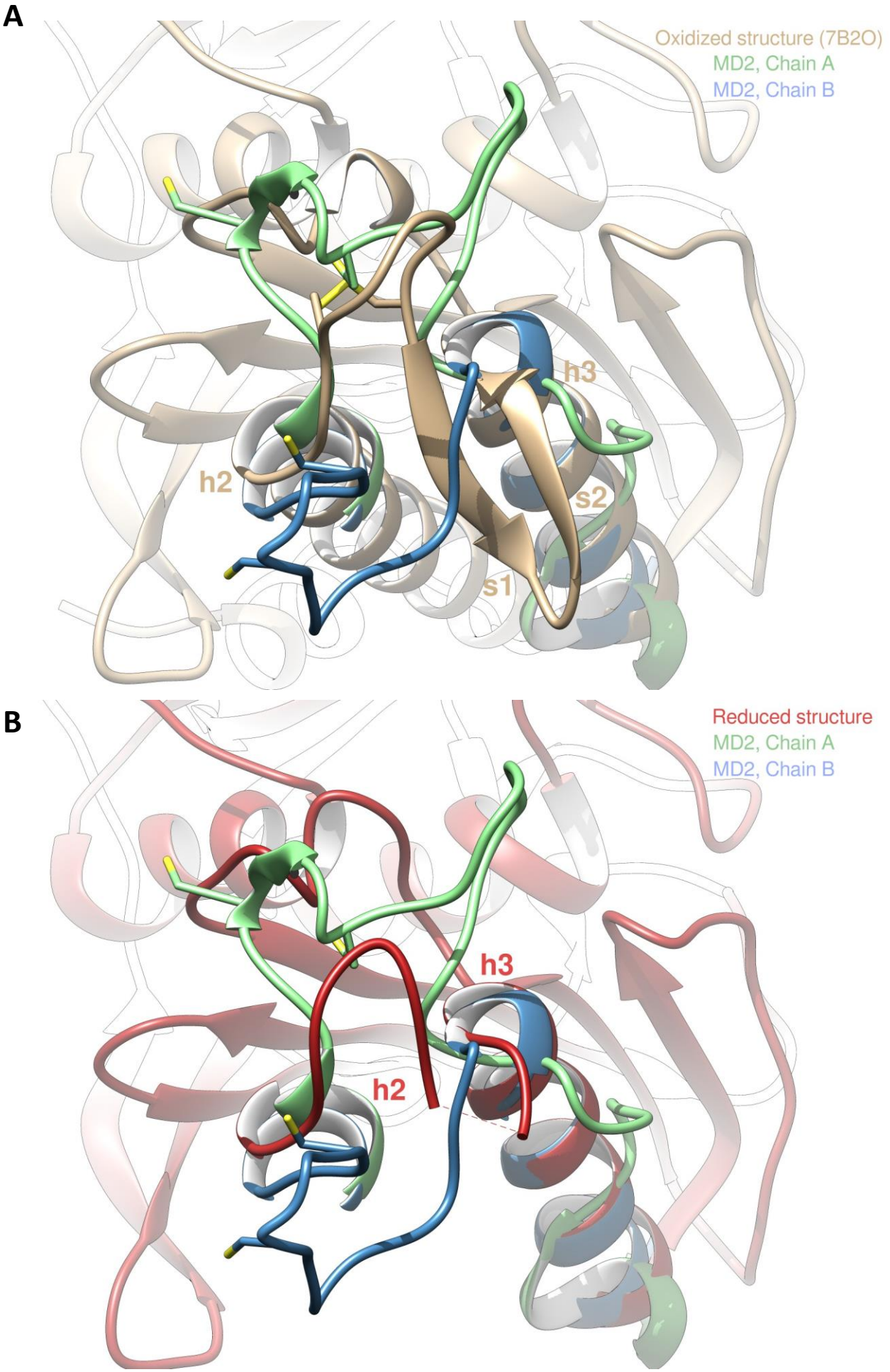
A
Oxidized structure (7B2O)
MD2, Chain A
MD2, Chain B
h3
h2
s2
s1
B
Reduced structure
MD2, Chain A
MD2, Chain B
h3
h2

Figure 5.

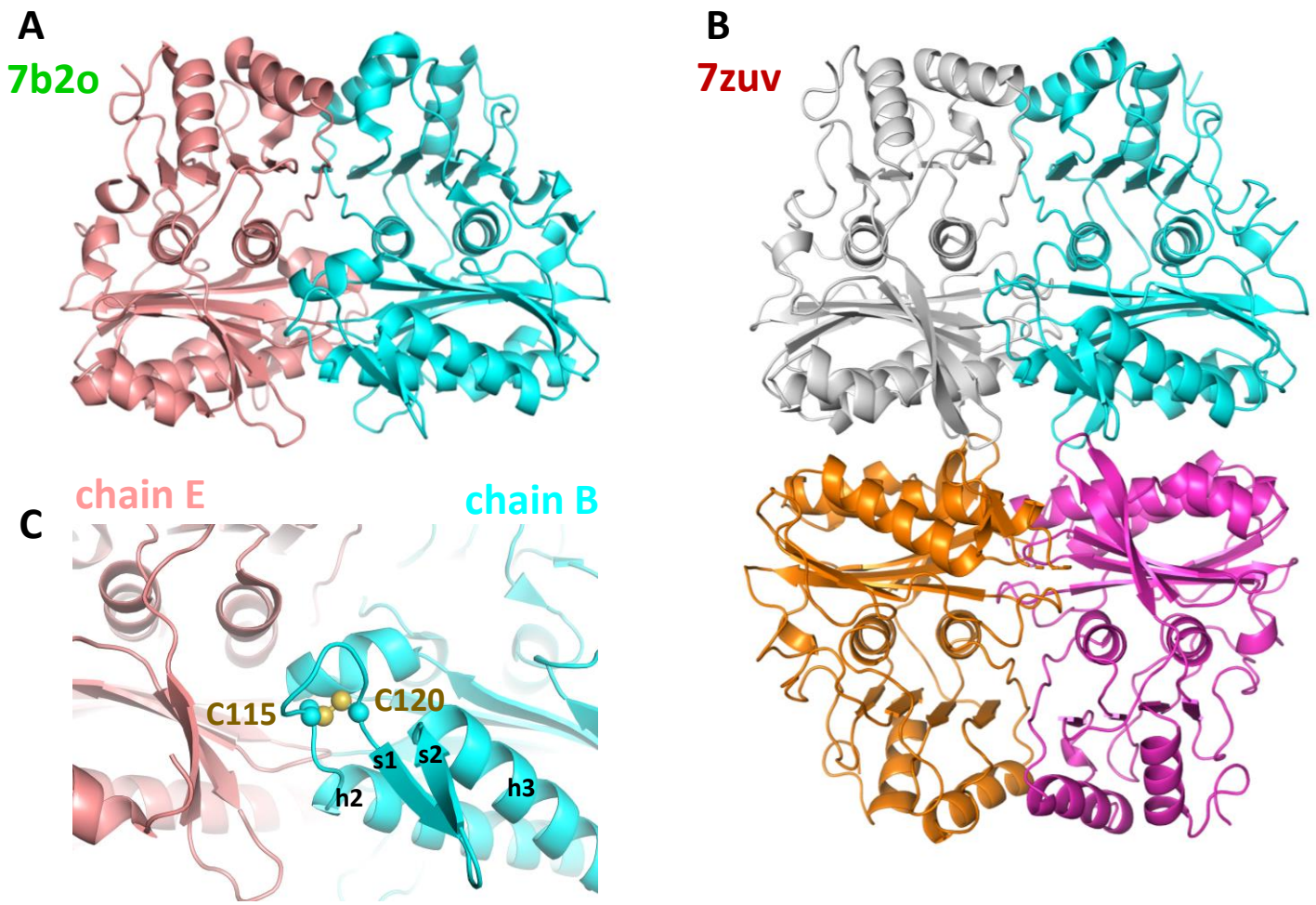

Figure 6.

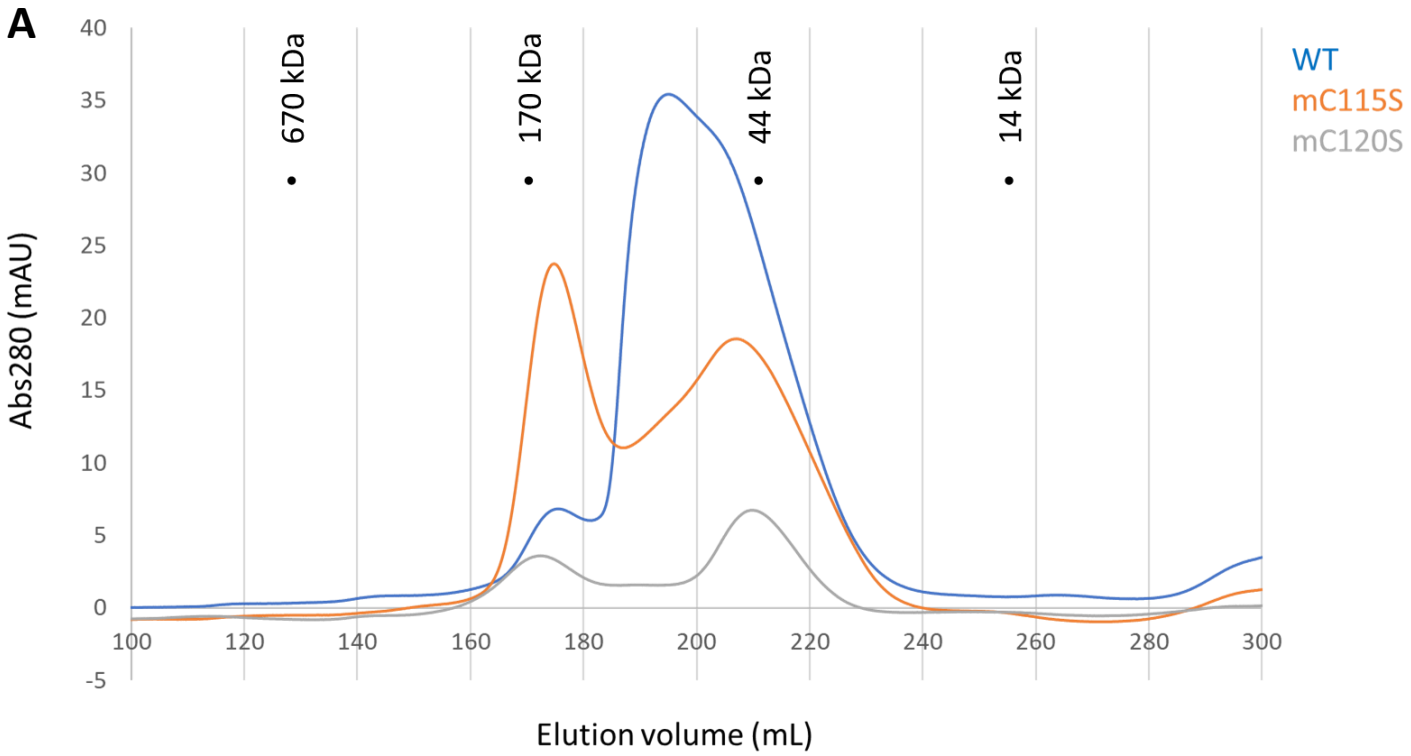
A
670 kDa
170 kDa
44 kDa
14 kDa
WT
mC115S
mC120S
Abs280 (mAU)
Elution volume (mL)

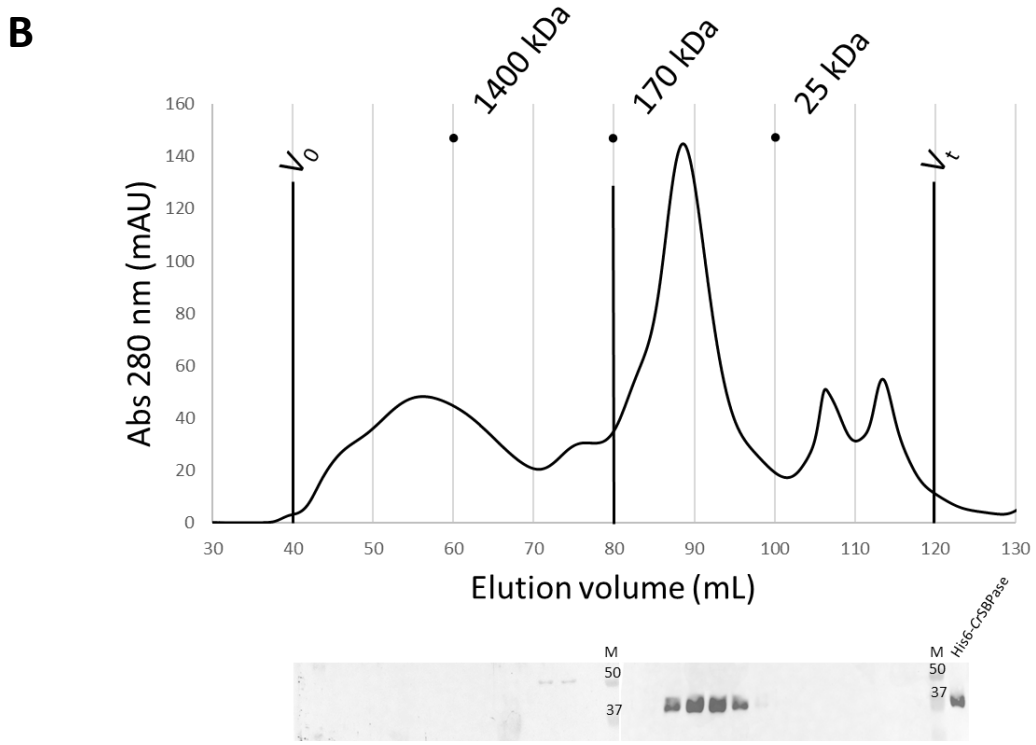
B
1400 kDa
170 kDa
25 kDa
V_o
V_t
Abs 280 nm (mAU)
Elution volume (mL)
M
50
37
M
50
37
His6-CrSBPase